Check for updates

Advanced Electronic Materials

ADVANCED ELECTRONIC MATERIALS Open Access

www.advelectronicmat.de

RESEARCH ARTICLE OPEN ACCESS

Stepwise Engineering of Van der Waals Heterostructures for High Current Density in Light Emitting Devices

Rei Usami[1] | Koshi Oi[1] | Keisuke Yamada[1] | Jiang Pu[2] | Hao Ou[1] | Takahiko Endo[3] | Yasumitsu Miyata[3,4] | Taishi Takenobu[1]

[1]Department of Applied Physics, Graduate School of Engineering, Nagoya University, Nagoya, Aichi, Japan | [2]Department of Physics, Institute of Science Tokyo, Tokyo, Japan | [3]Department of Physics, Tokyo Metropolitan University, Tokyo, Japan | [4]Research Center for Materials Nanoarchitectonics (MANA), National Institute for Materials Science (NIMS), Nagoya University, Tsukuba, Ibaraki, Japan

Correspondence: Taishi Takenobu (takenobu@nagoya-u.jp)

Received: 11 December 2024 | **Revised:** 19 April 2026 | **Accepted:** 25 May 2026

Keywords: electric double layer doping | light emitting device | Van der Waals heterostructure

ABSTRACT

Van der Waals (vdW) heterostructures of transition metal dichalcogenides (TMDs) have been widely employed in optoelectronic applications, including photodetectors, photovoltaic cells, and light-emitting devices (LEDs). Among these, PN-junction-based heterostructures are critical for advanced LED and laser applications, where achieving high current density is essential. However, the development of PN-junction-type LEDs using vdW heterostructures has been significantly hindered by the lack of effective doping techniques, resulting in devices with limited current densities. In this study, we propose a novel strategy for high-density carrier doping and reduced device resistance in vdW heterostructures by combining stepwise engineering of vdW stacking with electric double-layer (EDL) carrier doping. The stepwise-engineered heterostructure, based on WS_2/WSe_2, takes advantage of this configuration to facilitate efficient charge transport and enhanced carrier injection, as both P-type and N-type materials are in direct contact with the electrolyte, enabling high-density doping in both materials. Through EDL doping, clear electroluminescence was observed at the interface, with a peak current density of 9.4×10^4 A/cm^2. This result marks a significant advancement over previous reports, demonstrating a promising pathway toward vdW heterostructure-based laser applications.

1 | Introduction

The integration of dissimilar materials into heterostructures is essential for a wide range of electronic and optoelectronic applications [1, 2]. In particular, light-emitting devices (LEDs) based on PN junctions in semiconductor heterostructures are fundamental for advanced light sources and laser technologies [1–4]. Recently, the development of novel heterostructures using dangling-bond-free van der Waals (vdW) materials, which are not constrained by lattice mismatch, has been realized with semiconductor transition metal dichalcogenides (TMDs) [5–8]. These vdW heterostructures have enabled the fabrication of various functional devices, including PN junctions [9, 10], photovoltaic cells [11], and photodetectors [12]. However, most reports on TMD-based LEDs involve tunneling structures with hexagonal boron nitride tunneling layers [13–15]. In contrast, there are surprisingly few studies on pure PN junction-based LEDs made from TMD heterostructures, despite this being the standard device structure for cutting-edge light sources and laser applications [16–20]. One major challenge is the lack of effective doping methods for TMD semiconductors. Furthermore, although achieving high current density is crucial for laser applications, reports on current density in these devices remain scarce.

To address this issue, we focused on electrolyte-based electric double-layer (EDL) doping, which has been shown to achieve

This is an open access article under the terms of the Creative Commons Attribution License, which permits use, distribution and reproduction in any medium, provided the original work is properly cited.
© 2026 The Author(s). *Advanced Electronic Materials* published by Wiley-VCH GmbH

extremely high doping densities exceeding $10^{14}/cm^2$ [20–25]. This technique has enabled doping-induced phase transitions in semiconductor TMDs, such as ambipolar carrier transport and electric field-induced superconductivity—key phenomena for forming PN junctions and achieving high current density. Additionally, PN junction-type LEDs have been successfully fabricated using this doping method, with clear electroluminescence (EL) emissions observed in monolayer semiconductor TMDs [26–32], in-plane TMD heterostructures [33, 34], and out-of-plane vdW heterostructures [20]. These results strongly suggest that high current densities can be achieved through high-density EDL doping. However, directly applying EDL doping to vdW heterostructures presents challenges, as the emission position and area can shift with applied voltage, complicating the analysis of current densities [20].

To confront these challenges, we propose a novel device structure based on stepwise engineering of vdW heterostructures, combining EDL doping with a P-type WSe_2 monolayer and an N-type WS_2 monolayer. We observed non-linear current-voltage characteristics and fixed-position EL at the interface between WSe_2 and WS_2, confirming the formation of a PN junction through heterostructure design. Notably, the estimated current density reached 9.4×10^4 A/cm^2, presenting a new pathway for laser applications based on vdW heterostructures.

2 | Results and Discussion

2.1 | Proposed Device Architecture and Fabrication

Two-terminal LEDs based on EDL doping, known as electric-double-layer LEDs (EDLEDs), are unique devices that require only a luminescent material, a two-terminal electrode, and an electrolyte [31–33]. As illustrated in Figure 1a, by simply applying a voltage between the two electrodes, two types of EDL doping—one for holes and the other for electrons—are self-assembled on the semiconductor surface, leading to the formation of a PN junction and EL emission. This concept was first proposed for organic conjugated polymers [35–37] and has recently been extended to TMDs, including monolayers and in-plane heterostructures [31–34]. In this study, as shown in Figure 1b, we propose a device structure based on stepwise engineering, which incorporates an upper electrolyte and a lower staircase-shaped heterostructure of P- and N-type semiconductors. The electrolyte directly contacts both P- and N-type materials, which is essential for forming the EDL layer on the semiconductors. Notably, in monolayer and in-plane heterostructure EDLEDs, the light-emitting zone shifts depending on the applied voltage [31–34, 38], whereas vdW heterostructures with vdW gaps are expected to provide fixed-position light emission. This characteristic is advantageous for creating LEDs with optical resonators and future laser devices.

To fabricate a heterostructured PN junction, we selected a WSe_2 monolayer as the P-type semiconductor due to its strong P-type current in EDL transistors [38, 39]. Similarly, a WS_2 monolayer was chosen as the N-type semiconductor, owing to its significant N-type current in EDL transistors [38]. The target materials were single-crystalline triangular monolayers grown via chemical vapor deposition (CVD) [34], where the edges of the CVD-grown

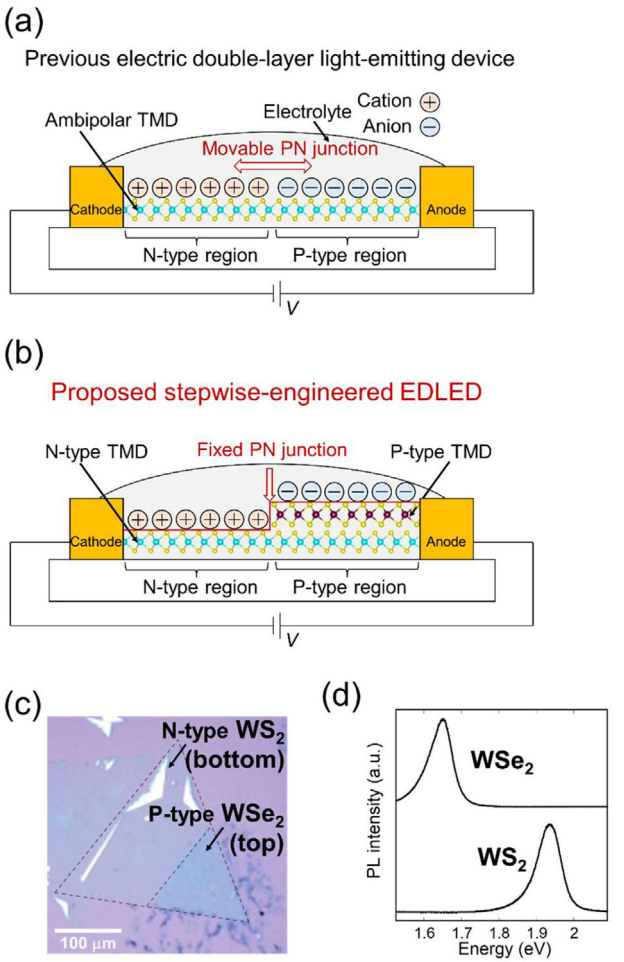


FIGURE 1 | Proposed device structure and fabrication of vdW heterostructure. Schematic representations of (a) the previous and (b) the proposed stepwise-engineered EDLEDs. (c) Optical micrograph of the fabricated vdW heterostructure, with P-type WSe_2 on top and N-type WS_2 on the bottom. The scale bar represents 100 μm. (d) PL spectra of WSe_2 (top) and WS_2 (bottom).

single crystals exhibit zigzag configurations [34, 40]. This feature enables precise control over the twist angle between the WSe_2 and WS_2 monolayers. As shown in Figure 1c, we aligned the zigzag edges of the single-crystal WSe_2 and WS_2 monolayers (twist angle = 0°), with the electrodes also aligned parallel to the zigzag edges. This ensures that carrier transport occurs in the armchair direction at the interface between WSe_2 and WS_2, facilitating efficient charge transfer across the junction.

To confirm the monolayer status of the samples, we collected photoluminescence (PL) spectra using a 532 nm laser (JASCO NRS-5100). The PL spectra shown in Figure 1d confirmed the monolayer nature of the materials [38]. Given that WSe_2 is typically smaller than WS_2, we selected the larger WS_2 monolayer, grown on a SiO_2/Si substrate, as the bottom layer. The smaller WSe_2 monolayer was then transferred onto the WS_2 layer. Finally, the ion-gel, composed of a triblock copolymer (poly(styrene-block-methyl methacrylate-block-styrene), PS-PMMA-PS; MPS = 4.3 kg/mol, MPMMA = 12.5 kg/mol, Mw = 21.1 kg/mol) and an ionic liquid, *N*, *N*-Diethyl-*N*-methyl-*N*-(2-methoxyethyl) ammonium bis(trifluoromethylsulfonyl)imide ([DEME][TFSI]),

21991160x, 2026, 16, Downloaded from https://advanced.onlinelibrary.wiley.com/doi/10.1002/aelm.202400930 by National Institute For, Wiley Online Library on [19/10/2026]. See the Terms and Conditions (https://onlinelibrary.wiley.com/terms-and-conditions) on Wiley Online Library for rules of use; OA articles are governed by the applicable Creative Commons License

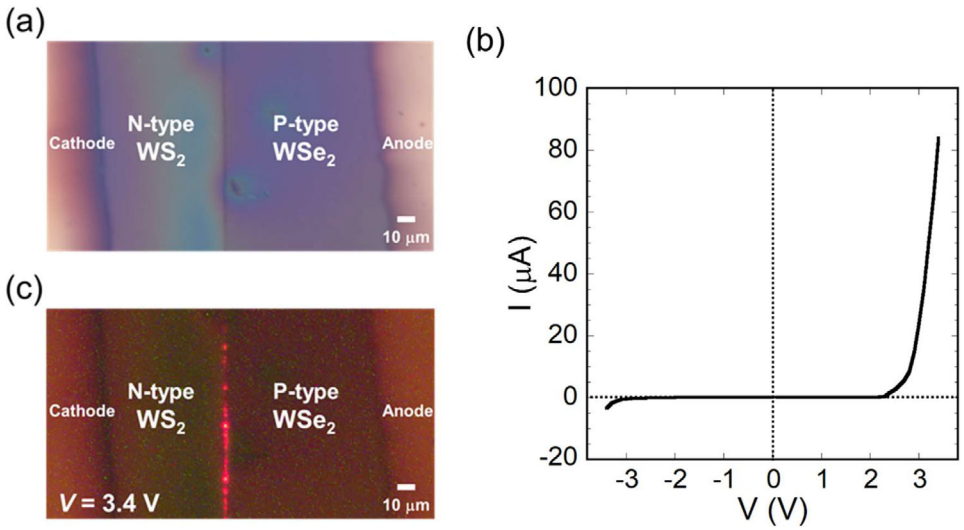


FIGURE 2 | Current-voltage characteristics and EL emission in vdW heterostructure of WS_2 and WSe_2. (a) Optical micrograph of the fabricated vdW heterostructure device, where the electrode on N-type WS_2 is the cathode, and the electrode on P-type WSe_2 is the anode. Scale bar: 10 μm. (b) Current-voltage characteristics of the vdW heterostructure composed of WS_2 and WSe_2. (c) Optical micrograph of the EL emission from the vdW heterostructure of WS_2 and WSe_2. Scale bar: 10 μm.

dissolved in ethyl propionate [31–37], was spin-coated onto the surface of the stepwise heterostructure at 6000 rpm for 120 s. The weight ratio of the copolymer, ionic liquid, and solvent was 0.7:9.3:90. For details on the optimized conditions, please refer to the Methods Section.

2.2 | Current–Voltage Characteristics and Electroluminescence

As shown in Figure 2a, the current (I)—voltage (V) characteristics were investigated with the electrode on the P-type WSe_2 as the anode and the electrode on the N-type WS_2 as the cathode, using a semiconductor parameter analyzer (Agilent Technologies, Inc. E5270) in a shielded probe station. All experiments were conducted in a glove box under a nitrogen atmosphere at room temperature. As shown in Figure 2b, we observed non-linear current-voltage characteristics for both forward and reverse bias, with clear rectification behavior. These results are consistent with those observed in EDL transistors, where the P-type current of the WSe_2 monolayer and the N-type current of the WS_2 monolayer are relatively larger than their opposite-charge counterparts, indicating the formation of a PN junction. To further confirm this, we observed the device under voltage application using a CCD camera (SHODENSHA) and a spectrometer (Hamamatsu Photonics K.K., Lambda Vision SA-100C-HPCB/C). Once again, all experiments were performed in a glove box under a nitrogen atmosphere at room temperature. As shown in Figure 2c, clear EL emission was observed at the WSe_2/WS_2 heterostructure interface at 3.4 V, confirming the formation of the PN junction at the WSe_2/WS_2 interface.

To gain a deeper understanding of the formation of the PN junction, we also investigated the transient current-voltage characteristics, as the dynamic response of ions is much slower than that of the hole and electron carriers. Based on previous reports on EDLEDs using monolayer TMDs [31, 32], we analyzed the I–V characteristics by dividing them into three distinct regimes and comparing their time-dependent currents, as shown in the logarithmic plot of the applied voltage (V) versus the absolute current ($|I|$) in Figure 3a.

First, as shown in Figure 3b, in regime (I) of Figure 3a, we observed a typical ion displacement current without a clear enhancement of the base current. This suggests the formation of EDL capacitors on the electrode surfaces. As illustrated in Figure 1a,b, applying an electric field redistributes anions and cations, forming EDLs on each electrode. These EDLs create a strong electric field and induce steeper band bending at the metal/TMD interfaces.

Next, in regime (II), shown in Figure 3c, two distinct contributions were observed. Similar to regime (I), one contribution was the ion displacement current, attributed to the formation of EDLs. In addition, a nonlinear increase in the base current was observed, indicating time-dependent conductivity enhancement in WSe_2 and/or WS_2 due to EDL capacitor formation. This suggests that in regime (II), an EDL doping layer is forming on the TMD surfaces. The relatively small enhancement in base current may indicate that the EDL doping primarily occurs in one of the TMDs, either WSe_2 or WS_2.

Finally, as shown in Figure 3d, in regime (III) of Figure 3a, a transient increase in current was observed. This large increase in transient current indicates the gradual spread of a 2D charge sheet and the formation of EDL capacitors on the surfaces of both WSe_2 and WS_2. This result is consistent with the observation of EL emission from the WSe_2/WS_2 heterostructure interface at 3.4 V, which corresponds to region (III). Notably, while these results qualitatively agree with those observed for EDLEDs using monolayer TMDs, the significant change between regimes (II) and (III) in Figure 3a is a unique feature of vdW heterostructures and strongly suggests the influence of the vdW gap (Section S1) [31, 32].

2199160x, 2026, 16, Downloaded from https://advanced.onlinelibrary.wiley.com/doi/10.1002/aelm.202400930 by National Institute For, Wiley Online Library on [19/10/2026]. See the Terms and Conditions (https://onlinelibrary.wiley.com/terms-and-conditions) on Wiley Online Library for rules of use; OA articles are governed by the applicable Creative Commons License

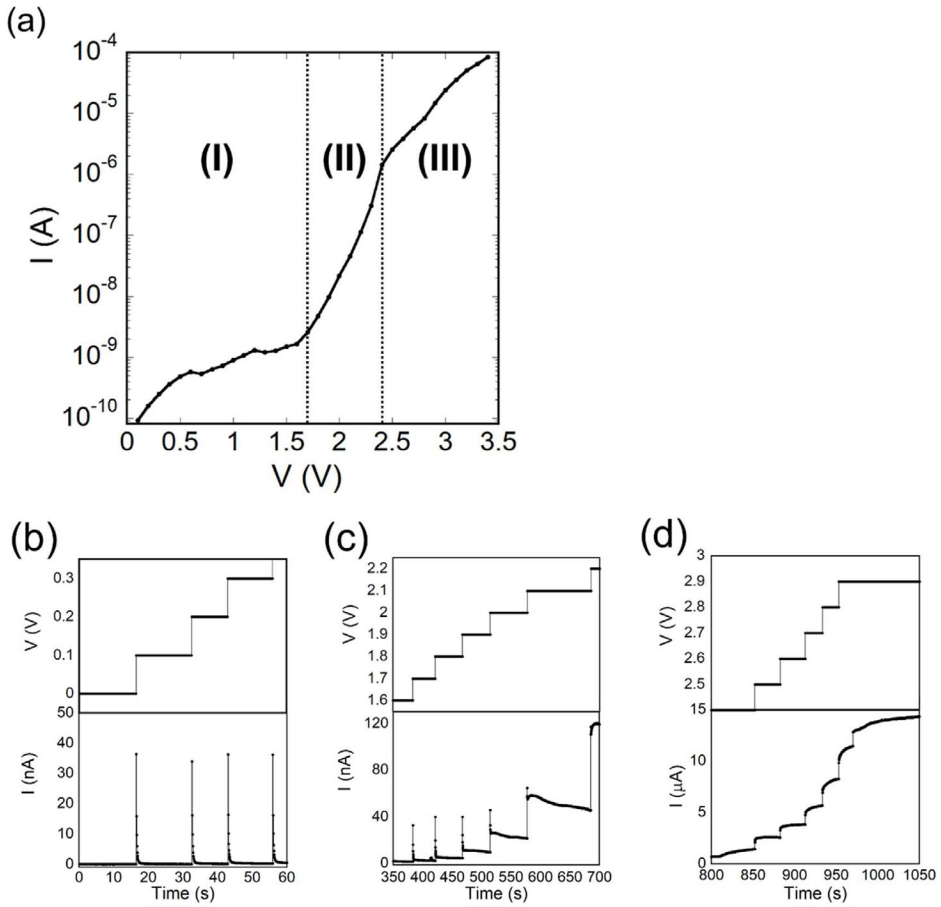


FIGURE 3 | Transient current-voltage characteristics in the vdW heterostructure of WS_2 and WSe_2. (a) Logarithmic plot of the applied voltage (V) dependence of absolute current ($|I|$). Transient current responses of the fabricated vdW heterostructure device under the application of constant voltage: (b) 0 V ≤ V ≤ 0.3 V, (c) 1.6 V ≤ V ≤ 2.2 V, and (d) 2.4 V ≤ V ≤ 2.9 V. These three transient behaviors correspond to regimes I, II, and III as defined in Figure 3a.

2.3 | Fixed-Position Electroluminescence Achieved Through Heterostructure Design

As mentioned above, clear EL emission was observed from the WSe_2/WS_2 heterostructure interface at 3.4 V, corresponding to regime (III). As illustrated in Figure 1b, this fixed EL emission aligns with the stepwise-engineered EDLED design. To further investigate, we examined the voltage dependence of the EL properties. As shown in Figure 4a, the EL intensity detected by the CCD camera increased with voltage from 2.9 to 3.4 V. Notably, the EL color and position remained almost constant, confirming fixed-position EL emission from the WSe_2/WS_2 heterostructure interface. It is important to note that in monolayer and in-plane heterostructure EDLEDs, the position of the light-emitting zone typically shifts with applied voltage (Section S2) [31–34, 38].

In monolayer and in-plane heterostructure EDLEDs, applying a voltage modifies not only the semiconductor region but also the EDL, leading to changes in the spatial distribution of carrier density within the sample. This dynamic redistribution causes the light-emitting zone to shift. In contrast, for WSe_2/WS_2 heterostructures, the vdW gap at the interface plays a critical role. The resistance of the vdW gap is significantly higher than that of the semiconductor regions, which causes the potential drop and the spatial distribution of carrier density to be predominantly determined by the vdW gap. Additionally, charge accumulation within the semiconductor regions requires the applied voltage to exceed the threshold voltage specific to each material. Since the threshold voltages of WSe_2 and WS_2 differ, charge sheets do not extend across the vdW gap. This prevents significant carrier redistribution across the interface and contributes to the fixed emission position. The combination of these effects—high vdW gap resistance and localized charge accumulation due to differing threshold voltages—ensures that the emission position remains pinned at the heterostructure interface, independent of the applied voltage. This behavior is particularly advantageous for applications requiring stable and localized light emission, such as optical resonators and laser devices.

To clarify the luminescence mechanism, we further analyzed the EL spectrum and compared it with the PL characteristics of the same sample. As shown in Figure 4b,c, the EL spectrum is much closer to the direct-gap emission of WS_2 than to that of WSe_2 or to the interlayer transition expected for the WS_2/WSe_2 heterostructure, strongly suggesting that the EL originates from WS_2. This observation appears inconsistent with the simple band alignment expected from theory. According to the reported band offsets for the WS_2/WSe_2 heterojunction [41], as shown

2199160x, 2026, 16, Downloaded from https://advanced.onlinelibrary.wiley.com/doi/10.1002/aelm.202400930 by National Institute For, Wiley Online Library on [19/10/2026]. See the Terms and Conditions (https://onlinelibrary.wiley.com/terms-and-conditions) on Wiley Online Library for rules of use; OA articles are governed by the applicable Creative Commons License

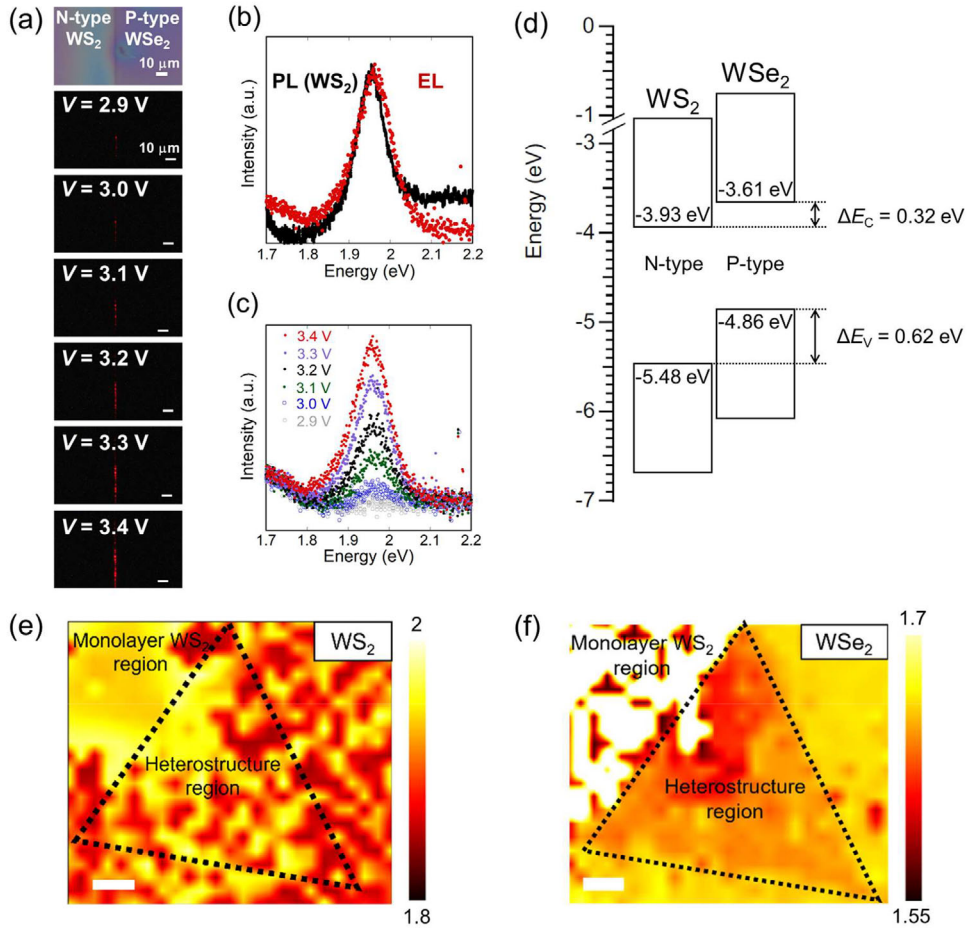


FIGURE 4 | EL properties in the vdW heterostructure of WS_2 and WSe_2. (a) Voltage dependence of the optical micrograph showing EL emission from the vdW heterostructure of WS_2 and WSe_2. The scale bar represents 10 μm. (b) EL spectrum (red) of the vdW heterostructure EDLED compared with the PL spectrum (black) of the WS_2 monolayer. (c) Voltage dependence of EL spectra. (d) Theoretical band profile of the WS_2/WSe_2 heterojunction. (e) WSe_2 PL peak mapping, (f) WS_2 PL peak mapping. The black dotted lines indicate the edge of top WSe_2 monolayer.

in Figure 4d, the conduction-band offset is $\Delta E_C = 0.32$ eV and the valence-band offset is $\Delta E_V = 0.62$ eV, which would suggest that recombination should occur more readily in WSe_2 than in WS_2.

To examine whether local variation of the bandgap could account for the observed WS_2 EL, we performed spatial mapping of the PL peak energies on the identical sample. As shown in Figure 4e,f, the observed PL peak energies ranged from 1.90 to 2.05 eV for WS_2 and from 1.61 to 1.64 eV for WSe_2. Although these values exhibit broader spatial variation than typically reported for pristine monolayer WS_2 and WSe_2, presumably due to local strain and/or transfer-induced inhomogeneity, the observed variation remains much smaller than the several-hundred-meV energy scale relevant to the interfacial injection asymmetry, as represented by the theoretically expected band offsets ($\Delta E_C = 0.32$ eV and $\Delta E_V = 0.62$ eV). Therefore, local bandgap variation alone cannot account for the reversal from the theoretically expected WSe_2-side recombination to the experimentally observed WS_2-origin EL. These results suggest that the dominant factor is not merely the intrinsic bandgap, but rather the effective carrier injection process across the heterointerface under high-density EDL doping.

A more plausible explanation is that the effective injection barrier is substantially modified by the strong local electric field formed across the van der Waals gap during operation. Previous studies on MoS_2/WSe_2 heterointerfaces have suggested that interfacial charge transfer can modify the electronic structure beyond the simple equilibrium band alignment expected from isolated monolayers [42]. In the present WS_2/WSe_2 device, such interfacial modulation may be further enhanced under high-density EDL doping, because electrons accumulated on the WS_2 side and holes accumulated on the WSe_2 side near the heterointerface can generate a strong local electric field across the van der Waals gap. This local field may substantially alter the effective band profile and the relative injection barriers during operation, thereby making hole injection into WS_2 more plausible than would be expected from the simple equilibrium band alignment.

Another, more speculative, possibility is that hole injection from WSe_2 to WS_2 is assisted by local metallization at the WSe_2 edge, analogous to edge metallization reported in other TMD systems such as MoS_2 and $MoSe_2$ [43, 44]. To the best of our knowledge, however, there is currently no direct experimental evidence for such a mechanism in WSe_2, and we therefore regard this only as a tentative possibility.

2199160x, 2026, 16, Downloaded from https://advanced.onlinelibrary.wiley.com/doi/10.1002/aelm.202400930 by National Institute For, Wiley Online Library on [19/10/2026]. See the Terms and Conditions (https://onlinelibrary.wiley.com/terms-and-conditions) on Wiley Online Library for rules of use; OA articles are governed by the applicable Creative Commons License

Further clarification of the dominant mechanism will require direct probing of the local potential profile and effective injection barrier near the heterointerface. In particular, Kelvin probe force microscopy would be a powerful method to examine local potential redistribution and band bending, while temperature-dependent EL and transport measurements would help distinguish between thermally activated injection and field-assisted or tunneling-like processes. Although the detailed recombination pathway remains to be clarified, the present results clearly indicate that the vdW heterointerface is responsible for the fixed-position EL, which is a unique feature of the stepwise vdW heterostructure.

As shown in Figure 4e, the PL peak energy exhibits clear spatial variation in the monolayer WS_2 region. Therefore, a comparison based on a single PL spectrum is not sufficient for discussing the spectral relationship between PL and EL. To obtain a more appropriate reference spectrum, we constructed the PL spectrum shown in Figure 4b by summing PL spectra extracted from multiple points in the monolayer WS_2 region as close as possible to the EL emission site near the WS_2/WSe_2 boundary. Based on this analysis, we find that the peak energy of the EL spectrum is in very good agreement with that of the corresponding PL spectrum.

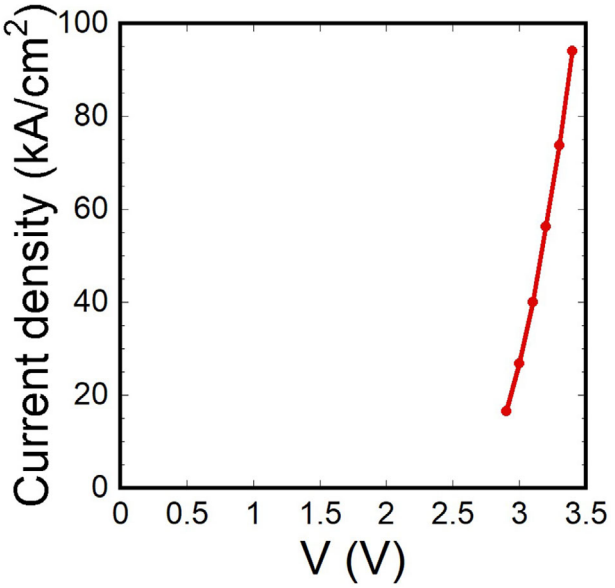


FIGURE 5 | Current density as a function of applied voltage in vdW heterostructure EDLEDs. The results demonstrate the characteristic *I–V* behavior of the device, highlighting the impact of the stepwise-engineered heterostructure.

2.4 | Achieving High Current Density in Stepwise-Engineered vdW Heterostructure EDLEDs

Finally, we estimated the current density in the stepwise-engineered vdW heterostructure EDLED. In this device, the stepwise design facilitates hole injection from the top WSe_2 layer into the bottom WS_2 layer, where hole–electron recombination occurs on the WS_2 side of the heterostructure interface. To calculate the current density, we defined the cross-section of the current path at the light-emitting zone as a rectangle formed by the WSe_2/WS_2 interface length (127.5 μm) and the WS_2 layer thickness (0.7 nm).

The resulting current density–voltage relationship in the voltage range of 2.9 to 3.4 V is shown in Figure 5. A maximum current density of 9.4×10^4 A/cm^2 was achieved, which is significantly higher than that of conventional laser diodes [45]. Additionally, as illustrated in Figure 3a, the device current increases dramatically by five orders of magnitude, from ~10^{-9} A at 1 V to ~10^{-4} A at 3.5 V. This substantial amplification strongly indicates that the stepwise-engineered structure and the formation of the EDL doping layer play crucial roles in achieving such high current density.

The proposed stepwise-engineered heterostructure is particularly advantageous because it enables direct contact with the electrolyte, forming efficient EDL doping layers for both the P- and N-type semiconductors. This design minimizes resistance throughout the device, except at the PN interface. These characteristics are pivotal for enhancing carrier injection and recombination efficiency.

To benchmark the present device, we compared the reported current densities of representative monolayer, few-layer, and heterostructure TMD light-emitting devices in the literature (Tables S1 and S2). This comparison highlights that electrolyte-gated devices generally reach much higher current densities than devices based on other doping schemes, and that the present WS_2/WSe_2 device is among the highest-current-density bilayer/heterostructure devices reported to date. A summary of the additional device statistics, including an additional WSe_2/WS_2 emitting device and the peak current-density distribution across stepwise heterostructure devices, is provided in Figures S3 and S4.

Although a quantitative evaluation of the EL efficiency is beyond the scope of the present study because the optical setup was not calibrated for absolute photon collection, previous studies on monolayer EDL emitters have shown that the EL efficiency is typically well below 1% [31, 32]. In this context, the observed increase in EL intensity with current, together with the absence of marked spectral broadening or degradation, suggests that radiative recombination remains operative at the heterointerface and that nonradiative loss and severe Joule heating do not dominate within the present operating range, although quantitative evaluation of the efficiency in the present heterostructure device will be an important subject for future work.

TMDs have already been combined with optical resonators to realize optically pumped lasing-related devices [46], and very recently electrically driven TMD laser operation has also been reported [47]. From this perspective, further development of TMD-based laser devices will benefit from electrically driven structures that are relatively simple, compatible with optical-cavity integration, and capable of sustaining both fixed-position emission and high current injection. The present stepwise-engineered heterostructure has these favorable features: a comparatively simple device structure, electroluminescence localized at a fixed heterointerface position, and high current density. These characteristics make the present architecture a promising platform for future integration with optical resonators and for exploring more advanced current-driven vdW heterostructure

2199160x, 2026, 16, Downloaded from https://advanced.onlinelibrary.wiley.com/doi/10.1002/aelm.202400930 by National Institute For, Wiley Online Library on [19/10/2026]. See the Terms and Conditions (https://onlinelibrary.wiley.com/terms-and-conditions) on Wiley Online Library for rules of use; OA articles are governed by the applicable Creative Commons License

light sources. More broadly, electrically driven high-injection operation assisted by electrostatic carrier accumulation has also been explored in other material systems [51, 52], suggesting that the present strategy may be relevant beyond the specific WS_2/WSe_2 heterostructure studied here.

3 | Conclusions

In this study, we proposed a novel and innovative strategy to achieve high current density in vdW heterostructure-based light-emitting devices. This strategy leverages a stepwise-engineered vdW stacking design combined with EDL carrier doping. The proposed device structure is remarkably simple, requiring only an electrolyte thin film deposited on the stepwise-engineered vdW stacking along with two electrodes. To demonstrate the effectiveness of this approach, we employed a WS_2/WSe_2 heterostructure, achieving an exceptionally high current density of approximately 0.1 MA/cm^2. Notably, the stepwise-engineered heterostructure enabled stable EL emission localized at a fixed position under a lateral bias. These findings underscore the significant potential of this device architecture for integration with optical resonators, opening new avenues for the realization of laser applications based on vdW heterostructures. We believe that this approach not only provides a pathway to enhance device performance but also contributes to the broader development of advanced optoelectronic technologies.

4 | Experimental Section

4.1 | Preparation of Van der Waals Heterostructures

The vdW stacks were fabricated using a polymer-assisted transfer method [48, 49]. As the polymer, we prepared Elvacite 2552C dissolved in anisole (weight ratio 1:1.5). Prior to sample collection, small drop of polymer was picked and transferred onto glass slide using a toothpick. The slide glass was then annealed at 180°C in air for 1 h. The polymer was first put into contact with the WSe_2 monolayer at 90°C, and the transfer stage was heated to 160°C to increase the contact area. Subsequently, the monolayer was picked up at 60°C. The polymer with WSe_2 monolayer was brought into contact with the WS_2 monolayer on Si/SiO_2 substrate at 170°C, at which the polymer would melt. By removing the substrate from the glass slide, part of the polymer was left on the substrate, with the WSe_2 monolayer. The residual polymer was then washed away by sequentially immersing the substrate in chloroform (2 min) and isopropyl alcohol (2 min). After fabricating the staircase-shaped heterostructure of WSe_2 and WS_2, Au/Ni electrodes (40/2.5 nm) were thermally deposited on both materials through the shadow mask.

4.2 | Optimization of Ion-Gel Films

The ion-gel composition strongly influences the film thickness, surface morphology, ionic conductivity, and mechanical stability, all of which affect the efficiency of EDL doping. According to our previous optimization study [50], increasing the solvent content and/or the ionic-liquid content relative to the polymer, as well as increasing the spin-coating speed, reduces the film thickness, whereas decreasing the ionic-liquid content lowers the ionic conductivity and makes the gel mechanically harder. In the present study, the composition and spin-coating conditions were chosen so that the film remained sufficiently thin and flat for stable optical measurements, while maintaining ionic conductivity high enough for effective EDL doping. The present ratio was selected as a practical balance among these competing requirements.

Acknowledgements

This work was financially supported by JSPS KAKENHI Grant Numbers JP20H05867, JP20H05664, JP21H05232, JP21H05234, JP21H05236, JP22H00280, JP22H04957, JP22KJ1555, JP22K19059, and JP22H01899, as well as by JST CREST Grant Numbers JPMJCR23A4 and JPMJCR23O3, Japan. H.O. acknowledges support from the JSPS Research Fellowship.

Conflicts of Interest

The authors declare no conflicts of interest.

Data Availability Statement

The data that support the findings of this study are available from the corresponding author upon reasonable request.

References

1. S. M. Sze, Y. Li, and K. K. Ng, *Physics of Semiconductor Devices* (Wiley, 2021).

2. H. Kroemer, "Heterostructure Bipolar Transistors and Integrated Circuits," *Proceedings of the IEEE* 70 (1982): 13–25, https://doi.org/10.1109/PROC.1982.12226.

3. H. Kroemer, "A Proposed Class of Hetero-junction Injection Lasers," *Proceedings of the IEEE* 51 (1963): 1782–1783, https://doi.org/10.1109/PROC.1963.2706.

4. C. W. Tang and S. A. VanSlyke, "Organic Electroluminescent Diodes," *Applied Physics Letters* 51 (1987): 913–915, https://doi.org/10.1063/1.98799.

5. A. K. Geim and I. V. Grigorieva, "Van der Waals Heterostructures," *Nature* 499 (2013): 419–425, https://doi.org/10.1038/nature12385.

6. K. S. Novoselov, A. Mishchenko, A. Carvalho, and A. H. Castro Neto, "2D Materials and Van der Waals Heterostructures," *Science* 353 (2016): aac9439, https://doi.org/10.1126/science.aac9439.

7. D. Jariwala, T. J. Marks, and M. C. Hersam, "Mixed-dimensional Van der Waals Heterostructures," *Nature Materials* 16 (2017): 170–181, https://doi.org/10.1038/nmat4703.

8. H. Ago, S. Okada, Y. Miyata, et al., "Science of 2.5 Dimensional Materials: Paradigm Shift of Materials Science Toward Future Social Innovation," *Science and Technology of Advanced Materials* 23 (2022): 275–299, https://doi.org/10.1080/14686996.2022.2062576.

9. C. H. Lee, G. H. Lee, A. M. van der Zande, et al., "Atomically thin p–n Junctions with Van der Waals Heterointerfaces," *Nature Nanotechnology* 9 (2014): 676–681, https://doi.org/10.1038/nnano.2014.150.

10. Y. Liu, N. O. Weiss, X. Duan, H.-C. Cheng, Y. Huang, and X. Duan, "Van der Waals Heterostructures and Devices," *Nature Reviews Materials* 1 (2016): 16042, https://doi.org/10.1038/natrevmats.2016.42.

11. O. Lopez-Sanchez, E. Alarcon Llado, V. Koman, A. Fontcuberta i Morral, A. Radenovic, and A. Kis, "Light Generation and Harvesting in a van der Waals Heterostructure," *ACS Nano* 8 (2014): 3042–3048, https://doi.org/10.1021/nn500480u.

2199160x, 2026, 16, Downloaded from https://advanced.onlinelibrary.wiley.com/doi/10.1002/aelm.202400930 by National Institute For, Wiley Online Library on [19/10/2026]. See the Terms and Conditions (https://onlinelibrary.wiley.com/terms-and-conditions) on Wiley Online Library for rules of use; OA articles are governed by the applicable Creative Commons License

12. S. J. Liang, B. Cheng, X. Y. Cui, and F. Miao, "Van der Waals Heterostructures for High-Performance Device Applications: Challenges and Opportunities," *Advanced Materials* 32 (2020): 1903800, https://doi.org/10.1002/adma.201903800.

13. F. Withers, O. Del Pozo-Zamudio, A. Mishchenko, et al., "Light-emitting Diodes by Band-structure Engineering in Van der Waals Heterostructures," *Nature Materials* 14 (2015): 301–306, https://doi.org/10.1038/nmat4205.

14. J. Wang, I. Verzhbitskiy, and G. Eda, "Electroluminescent Devices Based on 2D Semiconducting Transition Metal Dichalcogenides," *Advanced Materials* 30 (2018): 1802687, https://doi.org/10.1002/adma.201802687.

15. T. Ahmed, J. Zha, K. K. Lin, H.-C. Kuo, C. Tan, and D.-H. Lien, "Bright and Efficient Light-Emitting Devices Based on 2D Transition Metal Dichalcogenides," *Advanced Materials* 35 (2023): 2208054, https://doi.org/10.1002/adma.202208054.

16. R. Cheng, D. Li, H. Zhou, et al., "Electroluminescence and Photocurrent Generation from Atomically Sharp WSe_2 /MoS_2 Heterojunction p–n Diodes," *Nano Letters* 14 (2014): 5590–5597, https://doi.org/10.1021/nl502075n.

17. N. Balakrishnan, Z. R. Kudrynskyi, M. W. Fay, et al., "Room Temperature Electroluminescence from Mechanically Formed van der Waals III–VI Homojunctions and Heterojunctions," *Advanced Optical Materials* 2 (2014): 1064–1069, https://doi.org/10.1002/adom.201400202.

18. O. L. Sanchez, D. Ovchinnikov, S. Misra, A. Allain, and A. Kis, "Valley Polarization by Spin Injection in a Light-Emitting Van der Waals Heterojunction," *Nano Letters* 16 (2016): 5792–5797, https://doi.org/10.1021/acs.nanolett.6b02527.

19. J. S. Ross, P. Rivera, J. Schaibley, et al., "Interlayer Exciton Optoelectronics in a 2D Heterostructure p–n Junction," *Nano Letters* 17 (2017): 638–643, https://doi.org/10.1021/acs.nanolett.6b03398.

20. H. Henck, D. Mauro, D. Domaretskiy, et al., "Light Sources with Bias Tunable Spectrum Based on Van der Waals Interface Transistors," *Nature Communications* 13 (2022): 3917, https://doi.org/10.1038/s41467-022-31605-9.

21. J. T. Ye, Y. J. Zhang, R. Akashi, M. S. Bahramy, R. Arita, and Y. Iwasa, "Superconducting Dome in a Gate-Tuned Band Insulator," *Science* 338 (2012): 1193–1196, https://doi.org/10.1126/science.1228006.

22. H. T. Yuan, M. S. Bahramy, K. Morimoto, et al., "Zeeman-type Spin Splitting Controlled by an Electric Field," *Nature Physics* 9 (2013): 563–569, https://doi.org/10.1038/nphys2691.

23. D. Costanzo, S. Jo, H. Berger, and A. F. Morpurgo, "Gate-induced Superconductivity In Atomically Thin MoS_2 Crystals," *Nature Nanotechnology* 11 (2016): 339–344, https://doi.org/10.1038/nnano.2015.314.

24. J. Pu, L.-J. Li, and T. Takenobu, "Flexible and Stretchable Thin-film Transistors Based on Molybdenum Disulphide," *Physical Chemistry Chemical Physics* 16 (2014): 14996, https://doi.org/10.1039/c3cp55270e.

25. K. Yanagi, R. Moriya, Y. Yomogida, et al., "Electrochromic Carbon Electrodes: Controllable Visible Color Changes in Metallic Single-Wall Carbon Nanotubes," *Advanced Materials* 23 (2011): 2811–2814, https://doi.org/10.1002/adma.201100549.

26. Y. Zhang, T. Oka, R. Suzuki, J. T. Ye, and Y. Iwasa, "Electrically Switchable Chiral Light-Emitting Transistor," *Science* 344 (2014): 725–728, https://doi.org/10.1126/science.1251329.

27. S. Jo, N. Ubrig, H. Berger, A. B. Kuzmenko, and A. F. Morpurgo, "Mono- and Bilayer WS_2 Light-Emitting Transistors," *Nano Letters* 14 (2014): 2019–2025, https://doi.org/10.1021/nl500171v.

28. J. Pu and T. Takenobu, "Monolayer Transition Metal Dichalcogenides as Light Sources," *Advanced Materials* 30 (2018): 1707627, https://doi.org/10.1002/adma.201707627.

29. K. Matsuki, J. Pu, and T. Takenobu, "Recent Progress on Light-Emitting Electrochemical Cells with Nonpolymeric Materials," *Advanced Functional Materials* 30 (2020): 1908641, https://doi.org/10.1002/adfm.201908641.

30. J. Pu, K. Matsuki, L. Chu, et al., "Exciton Polarization and Renormalization Effect for Optical Modulation in Monolayer Semiconductors," *ACS Nano* 13 (2019): 9218, https://doi.org/10.1021/acsnano.9b03563.

31. J. Pu, T. Fujimoto, Y. Ohashi, et al., "A Versatile and Simple Approach to Generate Light Emission in Semiconductors Mediated by Electric Double Layers," *Advanced Materials* 29 (2017): 1606918, https://doi.org/10.1002/adma.201606918.

32. J. Pu, W. Zhang, H. Matsuoka, et al., "Room-Temperature Chiral Light-Emitting Diode Based on Strained Monolayer Semiconductors," *Advanced Materials* 33 (2021): 2100601, https://doi.org/10.1002/adma.202100601.

33. J. Pu, H. Ou, T. Yamada, et al., "Continuous Color-Tunable Light-Emitting Devices Based on Compositionally Graded Monolayer Transition Metal Dichalcogenide Alloys," *Advanced Materials* 34 (2022): 2203250, https://doi.org/10.1002/adma.202203250.

34. N. Wada, J. Pu, Y. Takaguchi, et al., "Efficient and Chiral Electroluminescence from In-Plane Heterostructure of Transition Metal Dichalcogenide Monolayers," *Advanced Functional Materials* 32 (2022): 2203602, https://doi.org/10.1002/adfm.202203602.

35. Q. Pei, G. Yu, C. Zhang, Y. Yang, and A. J. Heeger, "Polymer Light-Emitting Electrochemical Cells," *Science* 269 (1995): 1086–1088, https://doi.org/10.1126/science.269.5227.1086.

36. T. Sakanoue, J. Li, H. Tanaka, et al., "High Current Injection into Dynamic p–n Homojunction in Polymer Light-Emitting Electrochemical Cells," *Advanced Materials* 29 (2017): 1606392, https://doi.org/10.1002/adma.201606392.

37. T. Sakanoue, F. Yonekawa, K. Albrecht, K. Yamamoto, and T. Takenobu, "An Ionic Liquid that Dissolves Semiconducting Polymers: A Promising Electrolyte for Bright, Efficient, and Stable Light-Emitting Electrochemical Cells," *Chemistry of Materials* 29 (2017): 6122–6129, https://doi.org/10.1021/acs.chemmater.7b02128.

38. H. Ou, H. Matsuoka, J. Tempia, et al., "Spatial Control of Dynamic p–i–n Junctions in Transition Metal Dichalcogenide Light-Emitting Devices," *ACS Nano* 15 (2021): 12911–12921, https://doi.org/10.1021/acsnano.1c01242.

39. J. Pu, K. Funahashi, C.-H. Chen, M.-Y. Li, L.-J. Li, and T. Takenobu, "Highly Flexible and High-Performance Complementary Inverters of Large-Area Transition Metal Dichalcogenide Monolayers," *Advanced Materials* 28 (2016): 4111–4119, https://doi.org/10.1002/adma.201503872.

40. Y. Kobayashi, S. Yoshida, M. Maruyama, et al., "Continuous Heteroepitaxy of Two-Dimensional Heterostructures Based on Layered Chalcogenides," *ACS Nano* 13 (2019): 7527.

41. J. Kang, S. Tongay, J. Zhou, J. Li, and J. Wu, "Band Offsets and Heterostructures of Two-Dimensional Semiconductors," *Applied Physics Letters* 102 (2013): 012111.

42. M. H. Doan, Y. Jin, S. Adhikari, et al., "Charge Transport in MoS_2/WSe_2 Van der Waals Heterostructure with Tunable Inversion Layer," *ACS Nano* 11 (2017): 3832–3840, https://doi.org/10.1021/acsnano.7b00021.

43. Y. Xia, B. Wang, J. Zhang, et al., "Quantum Confined Tomonaga–Luttinger Liquid in Mo_6Se_6 Nanowires Converted From an Epitaxial $MoSe_2$ Monolayer," *Nano Letters* 20 (2020): 2094–2099, https://doi.org/10.1021/acs.nanolett.0c00090.

44. J. Dong, D. Ding, C. Jin, Y. Liu, and F. Ding, "Edge Reconstruction-Dependent Growth Kinetics of MoS_2," *ACS Nano* 17 (2022): 127–136, https://doi.org/10.1021/acsnano.2c05397.

45. K. S. Mobarhan, "Test and Characterization of Laser Diodes: Determination of Principal Parameters" Determination of Principal Parameter, https://www.laserdiodecontrol.com/laser-diode-parameter-overview.

46. S. Wu, S. Buckley, J. R. Schaibley, et al., "Monolayer Semiconductor Nanocavity Lasers with Ultralow Thresholds," *Nature* 520 (2015): 69–72, https://doi.org/10.1038/nature14290.

2199160x, 2026, 16, Downloaded from https://advanced.onlinelibrary.wiley.com/doi/10.1002/aelm.202400930 by National Institute For, Wiley Online Library on [19/10/2026]. See the Terms and Conditions (https://onlinelibrary.wiley.com/terms-and-conditions) on Wiley Online Library for rules of use; OA articles are governed by the applicable Creative Commons License

47. Z.-Z. Chen, H.-T. Lin, C.-Y. Chang, et al., "Electrically-Driven 2D Semiconductor Microcavity Laser," *Advanced Materials* 37 (2025): 09861, https://doi.org/10.1002/adma.202509861.

48. S. Masubuchi, M. Morimoto, S. Morikawa, et al., "Autonomous Robotic Searching and Assembly of Two-Dimensional Crystals to Build Van der Waals Superlattices," *Nature Communications* 9 (2018): 1413, https://doi.org/10.1038/s41467-018-03723-w.

49. H. Naito, Y. Makino, W. Zhang, et al., "High-throughput Dry Transfer and Excitonic Properties of Twisted Bilayers Based on CVD-grown Transition Metal Dichalcogenides," *Nanoscale Advances* 5 (2023): 5115–5121, https://doi.org/10.1039/D3NA00371J.

50. Y. Yomogida, J. Pu, H. Shimotani, et al., "Ambipolar Organic Single-Crystal Transistors Based on Ion Gels," *Advanced Materials* 24 (2012): 4392–4397.

51. S. Z. Bisri, K. Sawabe, M. Imakawa, et al., "Organic Single-Crystal Light-Emitting Transistor Coupling with Optical Feedback Resonators," *Scientific Reports* 2 (2012): 985.

52. K. Sawabe, T. Takenobu, S. Z. Bisri, T. Yamao, S. Hotta, and Y. Iwasa, "High Current Densities in a Highly Photoluminescent Organic Single-Crystal Light-Emitting Transistor," *Applied Physics Letters* 97 (2010): 043307, https://doi.org/10.1063/1.3466915.

Supporting Information

Additional supporting information can be found online in the Supporting Information section.

Supporting File: aelm70445-sup-0001-SuppMat.docx.

2199160x, 2026, 16, Downloaded from https://advanced.onlinelibrary.wiley.com/doi/10.1002/aelm.202400930 by National Institute For, Wiley Online Library on [19/10/2026]. See the Terms and Conditions (https://onlinelibrary.wiley.com/terms-and-conditions) on Wiley Online Library for rules of use; OA articles are governed by the applicable Creative Commons License